

Integrated Communication and Positioning Design in RIS-empowered OFDM Systems: A Correlation Dispersion Scheme

Xichao Sang, Lin Gui, *Member, IEEE*, Kai Ying, *Senior Member, IEEE*, Xiaqing Diao, and Derrick Wing Kwan Ng, *Fellow, IEEE*

Abstract—This paper proposes a novel reconfigurable intelligent surface (RIS)-aided integrated communication and positioning design for orthogonal frequency division multiplexing systems in indoor scenarios. A non-geometric strategy is employed to realize accurate positioning. Specifically, location-related information is embedded into channel frequency responses (CFR) and estimated through regular pilot subcarriers. The coefficients of RIS are optimized to maximize the norm of the CFR vector differences among users, exclusively considering physically adjacent users. To enhance positioning accuracy, we propose a two-stage framework that incorporates the prior information about the user in physical space. A unique feature, named “correlation dispersion”, within this framework is leveraged to enhance performance compared to geometric-based methods. By transforming the geometric prior information into the frequency domain capitalizing on Gaussian kernel method, we derive the Cramer-Rao Lower Bound (CRLB) of the proposed framework. A notable gain in CRLB is observed, highlighting the efficacy. Theoretical comparison with the CRLB of conventional methods validates the correlation dispersion property. Simulation results demonstrate a significant improvement in positioning accuracy when meticulously combining prior information with a non-geometric positioning method. Furthermore, our results unveil that the incorporation of rough positioning methods yields exceptionally high positioning performance, provided that the location information depicts different aspects.

Index Terms—Integrated communication and positioning, orthogonal frequency division multiplexing, reconfigurable intelligent surface, channel uncertainty, correlation dispersion

I. INTRODUCTION

In recent years, there has been a surge in research directed towards various wireless technologies, including millimeter wave (mmWave), massive multiple-input multiple-output (MIMO), and reconfigurable intelligent surfaces (RISs), aimed at enhancing the coverage, throughput, and energy/spectral efficiency for numerous emerging applications [1]. RISs, particularly, have garnered significant attention [2], [3], leveraging the programmability to facilitate information-bearing wireless signal propagation and giving rise to innovative concepts. Noteworthy among these are the smart radio environment [4] and the wireless environment as a service [5], [6], both flourishing

X. Sang, L. Gui, K. Ying, X. Diao are with the Department of Electronic Engineering, Shanghai Jiao Tong University, Shanghai 200240, China (email: sang_xc@sjtu.edu.cn; guilin@sjtu.edu.cn; yingkai0301@sjtu.edu.cn; xqdiao99@sjtu.edu.cn).

D. W. K. Ng is with the School of Electrical Engineering and Telecommunications, University of New South Wales, Sydney, NSW 2052, Australia (e-mail: w.k.ng@unsw.edu.au).

L. Gui is the corresponding author.

in the landscape of integrated sensing and communication (ISAC) [7]. It is widely anticipated that the introduction of RISs to wireless systems will enable dynamic electromagnetic wave control in the radio environment, facilitating customized services based on heterogeneous key performance indicators (KPIs) [5]. This development aligns perfectly with the future vision of location/environment-aware applications [8], e.g., seamless navigation transition, accurate indoor trajectory planning, as illustrated in Fig. 1. These applications are envisioned for beyond-fifth-generation (B5G) and sixth-generation (6G) wireless networks [9].

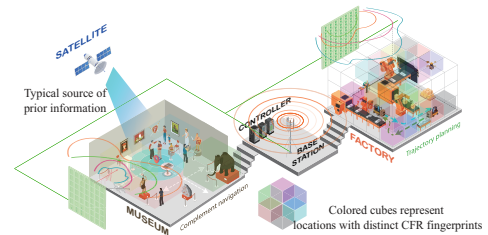


Fig. 1. Potential application scenarios with different KPIs.

As one of the most crucial elements of interconnecting and sensing, precise positioning is a key factor and an enabling technology for various use cases in the ISAC systems. In relation to this, the exploration of integrated communication and positioning (ICAP) has received extensive attention in both the academic and industrial sectors [10]–[15]. The fundamental principle of ICAP is grounded in the shared characteristic that both wireless communication and wireless positioning extract information from the traversing of electromagnetic beams and other signals [16]. As such, aligned with the promising design of ICAP for future wireless networks, substantial progress has been made in early research. Notably, the authors in [10] proposed a comprehensive resource allocation strategy for ICAP in mmWave frequency bands. This strategy involves estimating the angle-of-arrival (AoA) for positioning and developing a protocol for the allocation of time and frequency domain resources. To further enhance performance of the frequency selection strategy, the strategy in [11] improved the approach by considering the quality of service (QoS) of heterogeneous services, aiming at maximizing the overall transmission rate. Moreover, the authors in [12] utilized visible light communication (VLC) systems and exploited the detection of time-difference-of-arrival (TDoA) for positioning. It proved

that orthogonal frequency division multiplexing (OFDM)-based system was compatible with the triangulation positioning. More recently, a monocular resonant beam-based design was proposed in [13]. This design aims to improve the directivity of antenna beams, thereby enhancing positioning beyond VLC technology.

In the aforementioned integration explorations, the crux for achieving accurate positioning is the avoidance of complex multipath circumstances, as the indistinguishable link may attenuate accuracy. The authors exclusively assumed that the propagation process is dominated by line of sight (LoS), simplifying the abstraction of location-related information [10]–[13]. However, such an assumption is unrealistic, especially when dealing with practical wireless communication, as non-LoS links often offer additional gain to improve channel capacity. Among existing technologies, RIS, featured for reconfiguring the propagation process, introduces an additional degree of freedom (DoF) to harmonize these aspects of communication and positioning through the modulation of the propagation channel.

Leveraging the extra DoF provided by RIS, the authors in [17] circumvented blockages through the reflected link and treated RIS as an anchor to realize positioning through AoA estimate. By creating a strong and consistent multipath, RISs can support localization in even very harsh indoor environments. Inspired by the RIS’s ability to alleviate the impairment caused by multipath, the authors in [18] proposed a strategy to align all non-LoS links with the LoS to enhance the positioning accuracy. Moreover, the authors in [19] combined the traditional received signal strength (RSS)-based localization approach with RIS by designing a machine learning-based approach to select optimal RIS phases and artificially create fingerprint libraries to achieve localization. Also, the authors in [20], [21] used a probabilistic analytical-based approach to improve the localization accuracy by optimizing the localization error probability and dividing the localization process into multiple time slots.

While existing RIS-based designs showcase impressive positioning performance, typical RIS-aided methods still fall short of fully resolving the drawback imposed by multipath [17], [18]. The fundamental challenge stems from the fact that common positioning technologies, AoA, TDoA, time-of-arrival (ToA), and RSS, are geometric-based. This implies that the exact location is not directly obtained. Thus, as long as all the links, including LoS link and non-LoS links, are not fully exploited, there is a loss of information in positioning [22]. However, non-LoS links always introduce extra interference to positioning due to the existence of spatial consistency [23]. Here, spatial consistency or spatial correlation refers to the similarity in propagation that closely located users experience similar channel propagation effects. Notably, the fingerprint-based methods proposed in [19] and [21] provide an early exploration by considering all the channel information to construct a radio map. By collecting snapshots of every configuration of RIS, each location possesses a unique fingerprint for localization. The obtained information is not geometric-based, thus achieving even more precise localization benefiting from a different spatial correlation.

However, positioning through a series of modulations of

RIS in [19] and [21] represents a form of diversity in the time domain. Apart from being time-consuming, this approach may jeopardize the communication requirements of the inherent system. Furthermore, all the aforementioned RIS-aided positioning designs assume perfect channel state information (CSI) at the base station (BS), which is impracticable due to the limitations of the RF chain equipped at the RIS. A robust design approach assumption is often necessary, considering the time-varying nature of the location and the inherent inaccuracies in the channel estimate from RIS.

Therefore, in this paper, our objective is to propose a holistic RIS-aided ICAP design that seamlessly integrates communication and positioning functionalities in the presence of channel uncertainty. Built upon the concept that RIS can act as a spatial filter to mitigate the frequency selective fading and multipath effect [24], [25], we further investigate capability of RIS to reshape spatial correlation dispersion. We propose that RIS can be exploited to modulate the frequency characteristics of the radio environment by altering the spatial distribution of propagating waves. Based on the location-related information above, we design a two-stage positioning method with a single-time configuration of RIS instead of extensive searches across multiple time slots [19]–[21]. To be specific, the channel frequency response (CFR) of pilots of each place of interest (POI) that forms a vector can be treated as the corresponding virtual coordinate in the virtual positioning domain. That is to say, the exact location of the POI in the physical space is mapped into a virtual space through a linear transformation introduced by RIS. As such, the objective of minimizing the similarity of different CFRs is transformed into optimally designing the pattern of distribution of the virtual coordinates. We prove theoretically that the positioning accuracy is significantly improved through the combination of two positioning spaces that share distinct spatial consistency. The main contributions of this work are summarized as follows:

- We introduce a novel integrated communication and localization scheme in the context of a RIS-assisted OFDM communication system. RIS is leveraged to introduce enhanced location-related information. Notably, we enhance both communication and positioning function capability without additional resources or modifications to the transceiver system.
- A two-stage positioning framework that innovatively incorporates the prior information is proposed to enhance the positioning performance. A novel characteristic, named “correlation dispersion”, has been identified, indicating that the spatial consistency can be redesigned to construct a positioning-favor space with the help of RIS. This property enables extremely high positioning accuracy, particularly in low signal-to-noise ratio (SNR) conditions.
- Theoretical interpretation of the proposed correlation dispersion property is presented. The prior information is transformed into the frequency domain utilizing the Gaussian kernel method and the corresponding Cramér-Rao Lower Bound (CRLB) of the proposed positioning framework is derived. Compared to conventional geometric-based methods [20], our scheme exhibits a

significant reduction in CRLB.

- Simulation results validate the effectiveness of the proposed joint communication and localization scheme. The results demonstrate a great improvement in low-SNR conditions compared to conventional methods.

A. Organization & Notations

The rest of this paper is organized as follows. In Section II, we present the system model and formulate the problem of constructing the positioning space via a RIS. Section III introduces a general algorithm designed to address the non-convex optimization problem. Also, a novel property, termed ‘‘correlation dispersion’’, is firstly proposed. In Section IV, we derive the CRLB for the proposed positioning method and provide a theoretical interpretation of correlation dispersion. Simulation results are presented in Section V and Section VI concludes the paper.

The notations used in this paper are listed as follows. Upper and lower case boldface letters denote matrices and column vectors, respectively. $\mathbb{E}[\cdot]$ stands for statistical expectation. $\mathbb{C}^{M \times N}$ denotes the $M \times N$ complex-valued matrix. \mathbf{I}_M denotes the $M \times M$ identity matrix. For any general matrix \mathbf{A} , $A_{i,j}$ is the i -th row and j -th column element. \mathbf{A}^* , \mathbf{A}^T , and \mathbf{A}^H denote the conjugate, the transpose, and the conjugate transpose of \mathbf{A} , respectively. For any vector, \mathbf{x} (all vectors in this paper are column vectors), X_{i-1} is the i -th element. $\text{diag}(\mathbf{x})$ returns a diagonal matrix whose diagonal elements are included in \mathbf{x} , $\text{blkdiag}(\cdot)$ returns a block diagonal matrix created by aligning the input matrices or vectors. Reversely, $\text{Diag}(\mathbf{A})$ yields a vector containing the diagonal elements of matrix \mathbf{A} . $\mathbf{A} \succeq \mathbf{0}$ implies that \mathbf{A} is positive semidefinite. $\text{Tr}(\cdot)$ returns the trace of the matrix. $\text{rank}(\cdot)$ represents the rank of the input matrix. \circ denotes the element-wise produce. $\|\cdot\|_2$ and $\|\cdot\|_F$ denote the ℓ_2 -norm and the Frobenius norm, respectively. $|x|$ denotes the modulus of a complex number x .

II. SYSTEM MODEL AND PROBLEM FORMULATION

This paper investigates an indoor RIS-aided MISO-OFDM communication system, whose channel model follows the approach in [26]. The system structure is illustrated in Fig. 1, where the colored areas most likely to have users within the cell are designated as places of interest (POIs). These areas are divided into I distinct blocks. The centers of these blocks serve as the sampling locations, referred to as $\mathcal{I} = \{1, 2, \dots, I\}$. Typically, the features of received wireless signals serve as the basis of location distinction and determination for wireless indoor localization [27]. This paper adopts the concept of CFR fingerprints of users for positioning. The core idea of the fingerprint-based method involves matching a CFR vector in a database to an estimated CFR vector. Unlike traditional fingerprint measurements, which suffer from severe attenuation due to the multipath effects of signal propagation [28], the proposed RIS-aided positioning method focus on reshaping the multipath distribution, specifically the distribution of CFR. Our objective is to construct a communication-compatible fingerprint database with high resolution.

A. System Model

We consider a RIS-assisted transmission in the downlink, where a broadcast channel is employed. The system utilizes a RIS composed of M units of reflective elements, indexed by $\mathcal{M} = \{0, 1, \dots, M-1\}$, to modulate the transmission from a BS equipped with N_T antennas to K single-antenna users, denoted as $\mathcal{K} = \{0, 1, \dots, K-1\}$, requiring the same piece of information. The total bandwidth for transmission allocated to the users is uniformly divided into N orthogonal subcarriers, denoted by the index set $\mathcal{N} \triangleq \{0, 1, \dots, N-1\}$. Specifically, we define $\mathbf{h}_{k,n} \in \mathbb{C}^{N_T \times 1}$ and $\mathbf{G}_{k,n} \in \mathbb{C}^{N_T \times M}$ as the channel matrices representing the direct and the cascaded links, respectively, for the k -th user on the n -th subcarrier, $n \in \mathcal{N}$. The reflection performed on the m -th RIS element is to multiply the incident signals with θ_m , $m \in \mathcal{M}$, and then forward the composite signals, where $\theta_m = e^{-j\phi_m}$ denotes the reflection coefficient of the m -th element with phase shift $\phi_m \in (0, 2\pi]$.

At the BS side, we assume that the transmitted information across the N subcarriers is given by $\mathbf{s} = [s_0, s_1, \dots, s_{N-1}]^T \in \mathbb{C}^{N \times 1}$, satisfying $\mathbb{E}[\mathbf{s}\mathbf{s}^H] = \mathbf{I}_N$. Prior to transmission, the signal over N_T antennas on the n -th subcarrier is firstly digitally precoded by a beamforming vector as

$$\mathbf{x}_n = \mathbf{f}_n s_n, \quad (1)$$

where $\mathbf{f}_n \in \mathbb{C}^{N_T \times 1}$ is the beamforming vector on the n -th subcarrier. In this paper, our focus is to investigate the RIS’s potential for positioning. The beamforming of the antenna array will be determined using traditional methods such as maximum ratio transmission (MRT), minimum mean square error (MMSE) or other algorithms¹ [29], [30]. Subsequently, each OFDM symbol denoted by $\mathbf{X} = \text{blkdiag}([\mathbf{x}_0, \mathbf{x}_1, \dots, \mathbf{x}_{N-1}]) \in \mathbb{C}^{N N_T \times N}$ is first transformed into the time domain via an N -point inverse discrete Fourier transform (IDFT), and then appended with a cyclic prefix (CP) to avoid inter-symbol interference. At the user side, the received signal undergoes CP removal and is subjected to an N -point discrete Fourier transform (DFT) [31]. The received baseband signal at the k -th user, $k \in \mathcal{K}$, in the frequency domain over the N subcarriers is then given by

$$\mathbf{y}_k = \mathbf{X}^H \left(\tilde{\mathbf{G}}_k \boldsymbol{\theta} + \tilde{\mathbf{h}}_k \right) + \mathbf{n}_k. \quad (2)$$

We define $\tilde{\mathbf{G}}_k \triangleq [\mathbf{G}_{k,0}^H, \mathbf{G}_{k,1}^H, \dots, \mathbf{G}_{k,N-1}^H]^H \in \mathbb{C}^{N N_T \times M}$ and $\tilde{\mathbf{h}}_k \triangleq [\mathbf{h}_{k,0}^H, \mathbf{h}_{k,1}^H, \dots, \mathbf{h}_{k,N-1}^H]^H \in \mathbb{C}^{N N_T \times 1}$ as the concatenated channel matrix/vector for the cascaded links and direct link, respectively. $\boldsymbol{\theta} = [\theta_0, \theta_1, \dots, \theta_{M-1}]^T \in \mathbb{C}^{M \times 1}$ is the phase shifts vector of the RIS. We consider the presence of identical additive white Gaussian noise (AWGN) across different users and subcarriers as $\mathbf{n}_k \sim \mathcal{CN}(\mathbf{0}, \sigma_0^2 \mathbf{I}_N)$, where

¹This paper aims to explore the inherent positioning functionality facilitated by RIS and to assess the achievable positioning performance through RIS modulation. While dynamic beamforming techniques can introduce unpredictable channel fluctuations that may impact positioning, we employ a fixed beamforming scheme to exclusively investigate RIS-based positioning, ensuring a focused analysis. In the future work, we will extend to optimize both the phase shifts of RIS and precoders at the BS.

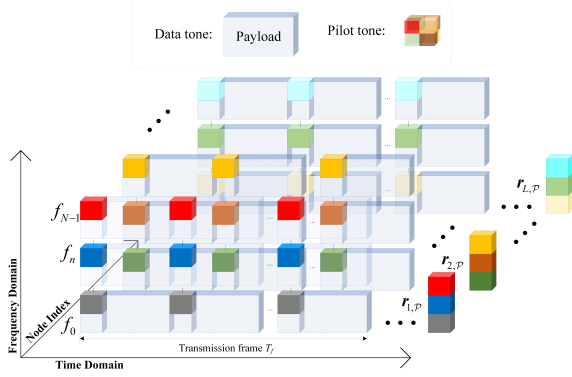


Fig. 2. Resource blocks with colored pilots.

σ_0^2 is power of noise on each subcarrier. In this way, the end-to-end designed channel frequency response (CFR) of the k -th user is represented as

$$\begin{aligned} \mathbf{r}_k &\triangleq [R_{k,0}, R_{k,1}, \dots, R_{k,N-1}]^T \\ &= \mathbf{F}^H \tilde{\mathbf{G}}_k \boldsymbol{\theta} + \mathbf{F}^H \tilde{\mathbf{h}}_k = \mathbf{F}^H \mathbf{G}'_k \boldsymbol{\theta}', k \in \mathcal{K}, \end{aligned} \quad (3)$$

where $\mathbf{F} \triangleq \text{blkdiag}(\{\mathbf{f}_0, \mathbf{f}_1, \dots, \mathbf{f}_{N-1}\}) \in \mathbb{C}^{N N_T \times N}$ is the beamforming matrix over all subcarriers. Augmented matrix $\mathbf{G}'_k \triangleq [\tilde{\mathbf{G}}_k, \tilde{\mathbf{h}}_k] \in \mathbb{C}^{N N_T \times (M+1)}$ and augmented vector $\boldsymbol{\theta}' \triangleq [\boldsymbol{\theta}^T, t]^T \in \mathbb{C}^{(M+1) \times 1}$ are introduced for ease of analysis in the sequel. Here, t is an auxiliary variable. Once the optimal solution is found, $\boldsymbol{\theta}$ can be recovered by $\boldsymbol{\theta} = \exp(\boldsymbol{\theta}'_{\mathcal{M}}/t)$.

To embed the positioning function through RIS, we leverage the existing training pilot sequence [22]. As illustrated in Fig. 2, we assume that a total of N_p pilots are uniformly inserted within each training OFDM symbol. These pilots are indexed by $\mathcal{P} = \{0, \Delta_p, \dots, (N_p-1)\Delta_p\}$, where $\Delta_p = \lfloor N/N_p \rfloor$ is the frequency spacing of adjacent pilots. By exploiting the public unit-power pilot sequence $\mathbf{s} \in \mathbb{C}^{N_p \times 1}$, it becomes possible to estimate the CFR of the k -th user on the pilot subcarriers \mathcal{P} . The corresponding subvector $\hat{\mathbf{r}}_{k,\mathcal{P}} \in \mathbb{C}^{N_p \times 1}$ that includes the CFR on pilot subcarriers is expressed as

$$\hat{\mathbf{r}}_{k,\mathcal{P}} = \mathbf{S}^{-1} \mathbf{y}_{k,\mathcal{P}} = \mathbf{r}_{k,\mathcal{P}} + \mathbf{S}^{-1} \mathbf{n}_{k,\mathcal{P}}, \quad (4)$$

where $\mathbf{S} = \text{diag}(\mathbf{s})$ is obtained by the diagonalization of the pilot sequence, and $\mathbf{y}_{k,\mathcal{P}} \in \mathbb{C}^{N_p \times 1}$ is the extracted received signal on pilot subcarriers. For ease of analysis, we assume that the updated noise follows isotropic distribution with unchanged power. In the subsequent discussion, with a slight abuse of notation, the subscript n is utilized consistently to denote the pilot index within \mathcal{P} . Consequently, CFR and the corresponding channel matrices are consistently referred to as the CFR on the pilot carriers, unless specified otherwise.

B. Two-Stage Positioning Framework

In this paper, we utilize the commonly adopted scaled- ℓ_2 -norm-with-log-probability for localization, which is derived from maximizing a posterior probability [32], expressed as

$$\begin{aligned} i_0 &= \arg \max_i P(\hat{\mathbf{r}}_{\mathcal{P}} | \mathbf{r}_{i,\mathcal{P}}) \\ \Leftrightarrow i_0 &= \arg \max_i \left[-\|\hat{\mathbf{r}}_{\mathcal{P}} - \mathbf{r}_{i,\mathcal{P}}\|_2^2 / \sigma_0^2 + 2 \log P(\mathbf{r}_{i,\mathcal{P}}) \right], \end{aligned} \quad (5)$$

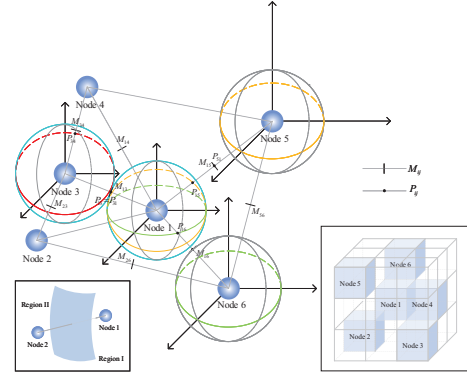


Fig. 3. Mapping from the physical domain to the topological domain.

where $\hat{\mathbf{r}}_{\mathcal{P}}$ is the estimated CFR vector through (4). $P(\mathbf{r}_{i,\mathcal{P}} | \hat{\mathbf{r}}_{\mathcal{P}})$ and $P(\mathbf{r}_{i,\mathcal{P}})$ are the posterior probability given the estimated CFR vector and the prior probability of the user at the i -th block, respectively. The prior information can be readily collected from previous estimates or GNSS [33], typically providing a coarse estimate. However, as both prior information and fingerprint data originate homogeneously from the geometric space, the prior information contributes limited distinctive location details. This homogeneity implies that inaccuracies in prior information align with those in fingerprint positioning, particularly in proximity to the given location.

To break through the limitation, we propose a two-stage framework. In the initial **prediction stage**, the prior information is employed to predict and narrow down the potential range of user locations over a certain confidence probability. Instead of pinpointing the exact location, we consider all locations within this confidence range without any bias. In the subsequent **correction stage**, we utilize the embedded CFR fingerprint information to determine the precise location among those within the confidence range established in the first stage. In particular, the distribution within the database of all fingerprints undergoes reorganization through RIS. This aims to exclude all potential locations that are physically close to the exact location so that the fingerprint information exhibits diverse spatial consistency compared to the prior information.

As exemplified in Fig. 3, each user's location are mapped into two spaces, i.e., the physical space and the virtual positioning space. Specifically the virtual positioning domain is constructed by treating the CFR subvector as the corresponding coordinate. For instance, the coordinate of a user at the i -th block is denoted as $(\mathbf{F}^H \mathbf{G}'_i \boldsymbol{\theta}')_{\mathcal{P}}$, where the operation $(\cdot)_{\mathcal{P}}$ yields the subvector or submatrix comprising of the elements or columns indexed by specified subcarriers. Note that these coordinates do not directly convey the geometric properties of the user's location. Instead, they serve as a mapping of the sample index $i \in \mathcal{I}$ to the positioning space. The dimension of the virtual positioning space is consistent with the dimension of CFR.

In Section IV, we will conduct an examination on the CRLB pertaining to the positioning scheme that integrates the prior information. Furthermore, we will demonstrate that the positioning performance of the proposed two-stage framework can achieve the corresponding CRLB.

C. Channel Uncertainty

Due to the limitations of RF chain equipped at RIS and signal processing capability in exploiting previous transmission slots for estimation, obtaining accurate CFR is challenging [34]. In this paper, we assume that the CFR estimated at the user side experiences some stochastic but bounded errors. By adopting a deterministic model, it becomes possible to characterize the channel model with inherent uncertainties as [35]:

$$\mathbf{G}'_k = \hat{\mathbf{G}}'_k + \Delta\mathbf{G}'_k, k \in \mathcal{K}, \quad (6)$$

$$\Omega_k \triangleq \left\{ \Delta\mathbf{G}'_k : \|\Delta\mathbf{G}'_k\|_F^2 = \sum_{n \in \mathcal{N}} \|\Delta\mathbf{G}_{k,n}\|_F^2 \leq \sum_{n \in \mathcal{N}} \epsilon_{k,n}^2 = \epsilon_k^2 \right\}, \quad (7)$$

where $\hat{\mathbf{G}}'_k$ denotes the estimate of the actual CSI, while $\Delta\mathbf{G}'_k$ and $\Delta\mathbf{G}_{k,n}$ represent random estimation errors of the channel matrix in (3) and cascaded channel of the k -th user on the n -th subcarrier, respectively. Non-negative factor ϵ_k and $\epsilon_{k,n}$ denote the bound of estimation uncertainty of $\Delta\mathbf{G}'_k$ and $\Delta\mathbf{G}_{k,n}$. Note that the LoS is perfectly estimated and the channel uncertainty assumption primarily pertains to the estimation error from the cascaded link. The set Ω_k is defined as a continuous set encompassing all potential CSI estimation errors, with their norms bounded by ϵ_k . We assume that the BS can acquire the knowledge of $\hat{\mathbf{G}}'_k$ and Ω_k , which refers to the estimates of the CSI and the corresponding uncertainty for the k -th user.

D. Problem Formulation

According to the positioning criterion in (5), a greater separation between any two physically close locations consistently results in better positioning accuracy. In the context of our proposed two-stage framework, a straightforward strategy involves expanding among locations within the potential area over the virtual positioning space. This ensures that each individual location can be accurately identified for a given energy of additive noise. As such, the subproblem of maximizing the worst-case positioning accuracy can be expressed as the mostly used ℓ_2 -norm of the coordinate differences:

$$\mathcal{P}_0: \max_{d, \theta'} \min_{\Delta\mathbf{G}', i, j} \|\mathbf{r}_{i, \mathcal{P}} - \mathbf{r}_{j, \mathcal{P}}\|_2^2, \quad (8)$$

where the minimization operation over the channel uncertainty aims to ensure an optimum for worst-case channel realizations.

Based on the primary focus of this paper to establish a RIS-aided integrated communication and positioning framework, our objective is to determine a set of optimal phase coefficients of RIS that maximizes positioning accuracy constrained by communication quality requirements. In the domain of RIS-aided communication, the optimization of the achievable data rate is a prevalent focus [36]. Based on the transmission system in this paper, the achievable data rate of the k -th user over N subcarriers can be expressed as:

$$C_k(\boldsymbol{\theta}) = \sum_{n \in \mathcal{N}} \log_2 \left(1 + \frac{W_{k,n}(\boldsymbol{\theta})}{\sigma_n^2} \right), \quad (9)$$

where $W_{k,n}(\boldsymbol{\theta}) \triangleq |\mathbf{f}_n^H(\mathbf{G}_{k,n}\boldsymbol{\theta} + \mathbf{h}_{k,n})|^2$ is the channel gain of the k -th user on the n -th subcarrier. The data rate, $C_k(\boldsymbol{\theta})$, is

measured in bits per second per Hertz (bps/Hz). To uphold the desired communication requirement, we impose a lower bound constraint for the achievable data rate [37] as $C_k(\boldsymbol{\theta}) \geq R_k$, where R_k is the minimum requirement.

To facilitate the optimization between communication and positioning, we introduce an auxiliary optimization variable, denoted as d , representing a lower bound for the mentioned ℓ_2 -norm in \mathcal{P}_0 . The optimization problem can then be formulated in the epigraph form as

$$\mathcal{P}_1: \max_{d, \theta'} d \quad (10)$$

$$\text{s.t. } \min_{\Delta\mathbf{G}'} \|\mathbf{r}_{i, \mathcal{P}} - \mathbf{r}_{j, \mathcal{P}}\|_2^2 \geq d, \forall i, j \in \mathcal{U}_i, \quad (10a)$$

$$\min_{\Delta\mathbf{G}'} C_k(\boldsymbol{\theta}) \geq R_k, \forall k \in \mathcal{K}, \quad (10b)$$

$$|\theta_m| = 1, \forall m \in \mathcal{M}, \quad (10c)$$

where the set \mathcal{U}_i includes those locations close to location i within a maximum physical distance of δ , exclude i itself. Here, δ is determined based on the confidence probability mentioned in the prediction stage of the proposed positioning framework. Based on the assumption that the additive noise is isotropically Gaussian distributed, the following equation holds:

$$\delta \triangleq \sqrt{2} \operatorname{erfc}^{-1} \left(\frac{1 - \sqrt[3]{\alpha}}{\sigma} \right), \quad (11)$$

where $\operatorname{erfc}^{-1}(\cdot)$ is the inverse function of the complementary error function. Note that the problem (\mathcal{P}_1) is positioning-centric, which aligns with the primary focus of this paper on assessing performance. The problem is challenging due to the infinite constraints arising from continuous channel uncertainty and the non-convex constraints (10b) and (10c). In the next sections, we will address these challenges by transforming the stochastic constraints into finite linear matrix inequalities (LMIs) and handling the non-convex constraint through approximation.

III. ALGORITHM DESIGN

A. Correlation Dispersion

In formulating the optimization problem, our focus is exclusively on the neighborhood of each location for positioning design. This selection aligns with the first phase of the proposed two-stage positioning framework, where we exclude the distant locations. For conventional geometric-based positioning methods [17], [18], inaccuracies in estimating locations among nearby areas always incur significant errors in positioning results. In contrast, locations farther away from that are less likely to contribute to significant mislocalization issues. Inspired by this observation, we propose the following proposition: the positioning accuracy will be significantly improved if there are different descriptions of location information that exhibit varied spatial consistency. We refer to the characteristic that reshapes the spatial consistency as ‘‘correlation dispersion’’.

In the first phase of our two-stage framework, we incorporate the geometric prior information to exclude physically separated locations. In the second phase, we aim to enhance the accuracy of localization in the vicinity of each point by prioritizing physically close locations in the virtual positioning space. Next, we qualitatively exemplify the correlation dispersion property and then theoretically prove it in Section IV.

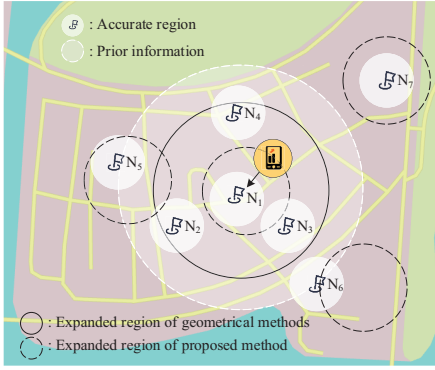


Fig. 4. Robust localization when affected with noise.

As depicted in Fig. 4, we aim to estimate the user's location within the range of N_1 under challenging situations. The white colored circles represent the accurate positioning zones with a 95% confidence probability for each block, while the circle with a white dashed border indicates the potential zone where the user is likely to appear based on the prior information. Conventional techniques such as angular estimating methods may encounter severe errors [15], causing the potential positioning range (circles with black solid borders) to expand, leading to a degradation in positioning accuracy. Such methods can only infer that the user's location is within the black-border circle without specific information about regions of N_2 , N_3 , or N_4 , making the prior information redundant.

By contrast, our proposed scheme smartly utilizes the prior information as an additional reference in another domain. Despite the potential positioning range (circles with black-dashed borders) expands due to noise, inaccuracy is dispersed into the entire virtual positioning space, as illustrated in Fig. 3. With the coarse prior information, we identify the user's location by considering the intersection of the white-dashed circle and the black-dashed circles. Consequently, maintaining or improving the accuracy in a challenging environment.

B. S-procedure

To handle the optimization problem, we first utilize matrix operations to express the channel difference matrix in a concise form as $\mathbf{D}_{ij} \triangleq \mathbf{D}_i - \mathbf{D}_j = \mathbf{F}^H(\mathbf{G}'_i - \mathbf{G}'_j)$. $\hat{\mathbf{D}}_{ij} \triangleq \hat{\mathbf{D}}_i - \hat{\mathbf{D}}_j$ and $\Delta\mathbf{D}_{ij} \triangleq \Delta\mathbf{D}_i - \Delta\mathbf{D}_j$ are defined in a similar manner. To characterize the uncertainty of channel difference matrices, we introduce Ω_{ij} defined as $\Omega_{ij} \triangleq \{\Delta\mathbf{D}_{ij} : \|\Delta\mathbf{D}_{ij}\|_F^2 \leq \hat{\epsilon}_{ij}^2\}$. Specifically, $\hat{\epsilon}_{ij}$ is obtained by

$$\begin{aligned} \|\Delta\mathbf{D}_{ij}\|_F^2 &= \|\mathbf{F}^H\Delta\mathbf{G}'_i - \mathbf{F}^H\Delta\mathbf{G}'_j\|_F^2 \\ &\stackrel{(a)}{\leq} \|\mathbf{F}^H\mathbf{G}'_i\|_F^2 + \|\mathbf{F}^H\mathbf{G}'_j\|_F^2 \\ &\stackrel{(b)}{\leq} \sum_{n \in \mathcal{N}} \|\mathbf{f}_n\|_2^2 \cdot \|\Delta\mathbf{G}_{i,n}\|_F^2 + \sum_{n \in \mathcal{N}} \|\mathbf{f}_n\|_2^2 \cdot \|\Delta\mathbf{G}_{j,n}\|_F^2 \\ &= \sum_{n \in \mathcal{N}} p_n(\epsilon_{i,n}^2 + \epsilon_{j,n}^2) \triangleq \hat{\epsilon}_{ij}^2, \end{aligned} \quad (12)$$

where p_n refers to the power allocation for the n -th subcarrier, satisfying $\sum_{n \in \mathcal{N}} p_n = 1$. Both inequalities (a) and (b) are valid according to the triangle inequalities of the Frobenius norm. Accordingly, we can convert the infinitely many constraints into equivalent forms with only a finite number of constraints. First, we reformulate (10a) into quadratic form as

$$\begin{aligned} (10a) &= \hat{\mathbf{D}}_{ij} \Theta \hat{\mathbf{D}}_{ij}^H + 2\Delta\mathbf{D}_{ij} \Theta \hat{\mathbf{D}}_{ij}^H \\ &\quad + \Delta\mathbf{D}_{ij} \Theta \Delta\mathbf{D}_{ij}^H - d\mathbf{I}_{N_p} \succeq \mathbf{0}, \forall \Delta\mathbf{D}_{ij} \in \Omega_{ij}, \end{aligned} \quad (13)$$

where $\Theta \triangleq \theta' \theta'^H$ is imparted as a substitution for the quadratic term. The equivalence holds on the condition of the following constraints:

$$|\theta_m| = 1 \iff \Theta \stackrel{\Delta}{=} \theta' \theta'^H \begin{cases} \text{Diag}(\Theta) = \mathbf{1}_{M+1}, \\ \text{rank}(\Theta) = 1, \\ \Theta \succ \mathbf{0}. \end{cases} \quad (14)$$

The introduced rank-one constraint still leaves the problem NP-hard and will be addressed later. Now, to tackle the infinite number of quadratic matrix inequalities (QMIs), we resort to the S-procedure Lemma [38, Proposition 3.4] to convert the constraints into a finite number of LMIs.

Lemma 1. *Given the bounded variable \mathbf{X} with $\text{Tr}(\mathbf{E}\mathbf{X}\mathbf{X}^H) \leq 1$, the following QMI*

$$\mathbf{X}^H \mathbf{A} \mathbf{X} + \mathbf{X}^H \mathbf{B} + \mathbf{B}^H \mathbf{X} + \mathbf{C} \succeq \mathbf{0}, \forall \mathbf{X} \quad (15)$$

holds if and only if there exists $q \geq 0$ such that

$$\begin{bmatrix} \mathbf{C} & \mathbf{B}^H \\ \mathbf{B} & \mathbf{A} \end{bmatrix} - q \begin{bmatrix} \mathbf{I}_n & \mathbf{0} \\ \mathbf{0} & -\mathbf{E} \end{bmatrix} \succeq \mathbf{0}, \quad (16)$$

where $\mathbf{A}, \mathbf{E} \in \mathbb{H}^{m \times m}$, $\mathbf{X}, \mathbf{B} \in \mathbb{H}^{m \times n}$, and $\mathbf{C} \in \mathbb{H}^{n \times n}$.

By substituting (14) into (16), the constraint is transformed accordingly as

$$\mathbf{S}_{ij}^{(a)} \Theta \mathbf{S}_{ij}^{(a)H} + \mathbf{Q}_{ij}^{(a)} \succeq \mathbf{0}, \quad (17)$$

where $\mathbf{S}_{ij}^{(a)} \triangleq [\hat{\mathbf{D}}_{ij}^H, \mathbf{I}_{M+1}]^H$ and $\mathbf{Q}_{ij}^{(a)} = \text{blkdiag}(- (q_{ij}^{(a)} + d)\mathbf{I}_{N_p}, q_{ij}^{(a)} \epsilon_{ij}^{-2} \mathbf{I}_{M+1})$. Here $q_{ij}^{(a)} \geq 0$ is an auxiliary variable.

The QoS constraint of (10b) is reformulated according to (14):

$$\min_{\Delta\mathbf{G}'_k} \sum_{n \in \mathcal{N}} \log_2 \left(1 + \frac{\mathbf{f}_n^H \mathbf{G}'_{k,n} \Theta \mathbf{G}'_{k,n}^H \mathbf{f}_n}{\sigma_n^2} \right) \geq R_k, k \in \mathcal{K}. \quad (18)$$

Although (18) is convex with respect to Θ , it involves infinitely many log-quadratic constraints due to the continuous channel uncertainty set. To handle this challenge, we introduce an auxiliary optimization $\gamma_{k,n}, k \in \mathcal{K}, n \in \mathcal{N}$, and reformulate the QoS constraint as

$$(18) \Leftrightarrow \begin{cases} \sum_{n \in \mathcal{N}} \log_2(1 + \gamma_{k,n}) \geq R_k, \\ \inf_{\Delta\mathbf{G}'_k} \{\mathbf{f}_n^H \mathbf{G}'_{k,n} \Theta \mathbf{G}'_{k,n}^H \mathbf{f}_n / \sigma_n^2\} \geq \gamma_{k,n}, \end{cases} \quad (19)$$

where $\inf\{\cdot\}$ returns the infimum of the set. The equivalence holds by exploiting the monotonicity of the logarithm function. It can be observed that the second set of inequalities of (20)

is also in the form of QMI and can be converted into a set of LMIs through the S-procedure. Specifically, the equivalent constraints can be expressed as

$$(20) \Leftrightarrow \mathbf{S}_{k,n}^{(b)} \boldsymbol{\Theta} \mathbf{S}_{k,n}^{(b)H} + \mathbf{Q}_{k,n}^{(b)} \succeq \mathbf{0}, k \in \mathcal{K}, n \in \mathcal{N}, \quad (21)$$

where $\mathbf{S}_{k,n}^{(b)} \triangleq [\hat{\mathbf{G}}'_{k,n} \mathbf{H} \mathbf{f}_n, \mathbf{I}_{M+1}]^H$ and $\mathbf{Q}_{k,n}^{(b)} = \text{blkdiag} \left(-(q^{(b)} + \gamma_{k,n} \sigma_n^2), q^{(b)} \epsilon_{k,n}^{-2} \mathbf{I}_{M+1} \right)$, while $q^{(b)} \geq 0$ is also an auxiliary variable.

C. Unit Modulus

In this subsection, we aim to solve the non-convex rank-one constraint introduced in (14). This constraint is crucial for maintaining an equivalence of the transformation but also leads to the NP-hard difficulty of the problem. To tackle this challenge, a common approach is to initially set aside the rank-one constraint and solve the problem as a convex optimization problem, i.e., semidefinite relaxation. Once an optimal solution is obtained, the rank-one solution is constructed using the Gaussian randomization method. However, this approach is computationally demanding and may not yield even a feasible solution to the original problem. Instead, we propose a heuristic successive convex approximation (SCA)-based method to improve the obtained rank-one solution iteratively. First, we rewrite the rank-one constraint in an equivalent form:

$$\text{rank}(\boldsymbol{\Theta}) = 1 \Leftrightarrow \|\boldsymbol{\Theta}\|_2 \geq M, \quad (22)$$

where $\|\boldsymbol{\Theta}\|_2$ represents the spectral norm of $\boldsymbol{\Theta}$, which is defined as the maximum singular value of $\boldsymbol{\Theta}$. It is important to note that the condition $\text{Diag}(\boldsymbol{\Theta}) = \mathbf{1}_M$ is crucial to ensure the equivalence, and it can be found in (14). Specifically, we utilize the property of matrices that the sum of eigenvalues is equal to the trace of the matrix. Therefore, the right-hand side term in the transformation originates from $\text{Tr}(\boldsymbol{\Theta}) = \sum_i \lambda_i \geq \max_i \{\lambda_i\}$, where equality holds if and only if $\boldsymbol{\Theta}$ has unit rank [39]. Here, λ_i is the i -th singular value of $\boldsymbol{\Theta}$. By introducing a lower bound on the spectral norm, we can enforce the rank-one constraint. However, the spectral norm is a convex function which makes the inequality constraint non-convex. To handle it, we first establish a lower bound of the spectral norm adopting its first-order Taylor expansion as follows:

$$\begin{aligned} \|\boldsymbol{\Theta}\|_2 &\geq \left\| \boldsymbol{\Theta}^{(t)} \right\|_2 \\ &+ \text{Tr} \left[\mathbf{v}^{(t)} \mathbf{v}^{(t)H} \left(\boldsymbol{\Theta} - \boldsymbol{\Theta}^{(t)} \right) \right] \text{Tr} \left(\mathbf{v}^{(t)} \mathbf{v}^{(t)H} \boldsymbol{\Theta} \right), \end{aligned} \quad (23)$$

where $\mathbf{v}^{(t)}$ is the eigenvector in the t -th iteration of SCA corresponding to the maximum eigenvalue of $\boldsymbol{\Theta}^{(t)}$ from the last iteration, we can obtain a convex approximation constraint as follows

$$\text{Tr} \left(\mathbf{v}^{(t)} \mathbf{v}^{(t)H} \boldsymbol{\Theta} \right) \geq M. \quad (24)$$

As such, a convex approximation of the non-convex rank-one constraint is constructed.

Algorithm 1 Map Construct Algorithm

Input: channel matrices \mathbf{G}_k with errors, for all $i \in \mathcal{I}$; initiate $\boldsymbol{\Theta}^{(0)}$ with random phase.

Output: output optimal $\boldsymbol{\theta}_o$

- 1: Set iteration index $r = 0$;
 - 2: Calculate \mathbf{D}_{ij} by channel matrices;
 - 3: **repeat**
 - 4: Solve problem \mathcal{P}_2 for given $\boldsymbol{\Theta}^{(r)}$, to update $\boldsymbol{\Theta}^{(r+1)}$
 - 5: Given $r + 1$ for $\boldsymbol{\Theta}^{(r+1)}$, obtain the eigenvector $\mathbf{v}^{(t+1)}$ corresponding to the largest eigenvalue;
 - 6: Update the penalty factor ϱ ;
 - 7: Update $r \leftarrow r + 1$;
 - 8: **until** $|d^{(r+1)} - d^{(r)}| \leq \varepsilon$; obtain the optimal $\boldsymbol{\Theta}_o$
 - 9: Decompose $\boldsymbol{\Theta}_o = \tilde{\boldsymbol{\theta}}_o \tilde{\boldsymbol{\theta}}_o^H$, obtain $\boldsymbol{\theta}_o = \tilde{\boldsymbol{\theta}}_{o,\mathcal{M}} / \tilde{\boldsymbol{\theta}}_o(\text{end})$.
-

Then, we employ a penalty-based method inspired by [40], [41] to enforce the transformed rank-one constraint. Specifically, we augment a penalty term to the objective function as

$$f(d, \boldsymbol{\Theta}) = -d + \frac{1}{\varrho} \left(\text{Tr} \left(\mathbf{v}^{(t)} \mathbf{v}^{(t)H} \boldsymbol{\Theta} \right) - M \right), \quad (25)$$

where $\varrho \rightarrow 0^+$ is a penalty factor that penalizes the violation of the rank-one constraint. By adopting the aforementioned transformation and approximation, the original optimization problem is then converted into

$$\mathcal{P}_2: \min_{d, \boldsymbol{\Theta}, \gamma_{k,n}} f(d, \boldsymbol{\Theta}) \quad (26)$$

$$\text{s.t. } \text{Diag}(\boldsymbol{\Theta}) = \mathbf{1}_M; \boldsymbol{\Theta} \succeq \mathbf{0}, \quad (26a)$$

$$(17), (19), (21). \quad (26b)$$

The optimization problem \mathcal{P}_2 is converted into a standard convex semi-definite program (SDP) and hence can be optimally solved by existing convex optimization programming solvers such as CVX [42]. The overall algorithm proposed in this section is summarized in **Algorithm 1**. By iteratively adjusting the penalty factor and solving the converted optimization problem \mathcal{P}_2 , we can monotonically decrease the value of the objective. In this way, the matrix of the coefficients of RIS converges to a stationary point to \mathcal{P}_2 in polynomial time [43]. Furthermore, the computational complexity of each iteration of the proposed algorithm is given by $\mathcal{O} \left(\log \frac{1}{\varepsilon} \sqrt{M+1} (K^2 N^2 M^2 + K^3 N^3) \right)$ [44, Th. 3.12], where \mathcal{O} is the big-O notation.

IV. CRLB ANALYSIS

In the last section, we qualitatively highlight the characteristic called ‘‘correlation dispersion’’. In this section, we focus on a mathematical interpretation of this characteristic through statistical analysis. Our objective is to derive the CRLB for the proposed positioning framework.

We omit the block division in Section II to explore the continuous bound of positioning performance. In our work, we incorporate some prior information to achieve effective positioning, wherein localization is essentially realized based on two sources of positioning information. For a user located at $\mathbf{p}_0 = [x_0, y_0, z_0]$, the prior knowledge can be readily

obtained through prediction or rough positioning methods and be modelled as Gaussian distribution [45]:

$$f(\mathbf{p}) = \frac{1}{(2\pi)^{\frac{3}{2}} \det^{\frac{1}{2}}(\boldsymbol{\Sigma}_0)} \exp\left(-\frac{1}{2}(\mathbf{p} - \mathbf{p}_0)^T \boldsymbol{\Sigma}_0^{-1}(\mathbf{p} - \mathbf{p}_0)\right), \quad (27)$$

where $\boldsymbol{\Sigma}_0 \in \mathbb{R}^{3 \times 3}$ represents the covariance matrix (usually large in terms of positive definiteness). On the other hand, the information provided by the CFR positioning method can be expressed as circularly symmetric complex Gaussian distribution:

$$f(\mathbf{r}) = \mathcal{CN}_{\Gamma_0}(\mathbf{r} - \mathbf{r}_0), \quad (28)$$

where $\mathcal{CN}(\mathbf{x}) = \frac{1}{\pi^{N_p} \det(\mathbf{A})} \exp(-\mathbf{x}^H \mathbf{A}^{-1} \mathbf{x})$ is the probability density function (pdf) of complex Gaussian distribution with covariance matrix \mathbf{A} . The two distributions describe distinct aspects for the user at location \mathbf{p}_0 and need to be harmonized in the same domain for further analysis. To reveal the advantage of integrating RIS, we opt to convert the prior knowledge (27) into the CFR domain. This transformation is systematically executed through a mapping function $\mathbf{r} = \mu(\mathbf{p})$ that establishes relationship between physical locations and positioning parameters, often involving angles and distances. However, with the introduction of RIS, exact expression can be intricate due to multiple links and may vary with different reflection coefficients of the RIS.

As illustrated in Fig. 3, there is no straightforward connection between the physical space and the positioning space. Even with a known closed-form expression for $\mu(\cdot)$, evaluating $g(\mathbf{r}_0) = f(\mu^{-1}(\mathbf{r}_0))$ can be extremely computationally demanding. To address this challenge, we employ the kernel density estimator technique [46] to estimate the distribution of the prior information in the CFR domain. Specifically, the commonly adopted kernel density estimation assumes that the probability density is a smoothed version of the empirical samples. For a collection of M measured data samples $\{\mathbf{r}_i\}_{i=1}^M$, the estimate $\hat{g}(\mathbf{r})$ of the underlying pdf $g(\mathbf{r})$ is the average of radial kernel functions centered on the $L + 1$ measured data samples

$$\hat{g}(\mathbf{r}) = \frac{1}{L+1} \sum_{i=0}^L K(\mathbf{r} - \mathbf{r}_i). \quad (29)$$

Here, we assume $K(\cdot)$ to be a complex-valued Gaussian kernel:

$$K(\mathbf{r}) = \mathcal{CN}_{\boldsymbol{\Sigma}}(\mathbf{r}), \quad (30)$$

and its covariance matrix (or kernel width) [46], is defined as $\boldsymbol{\Sigma}$. As $L \rightarrow \infty$, it can be demonstrated that $\hat{g}(\mathbf{r})$ converges to the true density under certain conditions [47]. For the empirical samples in (29), we choose L locations that are physically close to the expected location \mathbf{r}_0 . For example, if N_1 in Fig. 4 seeks localization through GNSS, $N_2 \sim N_4$ are considered the relevant samples.

We adopt the log-linear pooling [48] to aggregates the two opinions using a geometric average:

$$h(\mathbf{r}) = \frac{f(\mathbf{r}) \cdot \hat{g}(\mathbf{r})}{\int_{\mathcal{C}} f(\mathbf{r}) \cdot \hat{g}(\mathbf{r}) d\mathbf{r}}. \quad (31)$$

The form of $h(\mathbf{r})$ can be derived with the following lemma.

Lemma 2. *The pdf of the renewed distribution is given by $(L + 1)$ -term Gaussian mixture*

$$h(\mathbf{r}) = \sum_{i=0}^L w_i \cdot \mathcal{CN}_{\mathbf{E}}(\mathbf{r} - \mathbf{e}_i), \quad (32)$$

where the weight w_i , the positive definite matrix \mathbf{E} , and the $N_p \times 1$ vector \mathbf{e}_i is defined as

$$w_i = \frac{\mathcal{CN}_{\mathbf{C}}(\mathbf{r}_0 - \mathbf{r}_i)}{\sum_{j=0}^L \mathcal{CN}_{\mathbf{C}}(\mathbf{r}_0 - \mathbf{r}_j)}, \quad (33)$$

$$\mathbf{C} = \boldsymbol{\Sigma} + \Gamma_0, \mathbf{E} = \Gamma_0(\Gamma_0 + \boldsymbol{\Sigma})^{-1}\boldsymbol{\Sigma}, \mathbf{E}^{-1}\mathbf{e}_i = \Gamma_0^{-1}\mathbf{r}_0 + \boldsymbol{\Sigma}^{-1}\mathbf{r}_i. \quad (34)$$

Proof. The key of Lemma 2 is the proof of the following identify

$$\mathcal{CN}_{\boldsymbol{\Sigma}}(\mathbf{r} - \mathbf{r}_i) \cdot \mathcal{CN}_{\Gamma_0}(\mathbf{r} - \mathbf{r}_0) = \mathcal{CN}_{\mathbf{E}}(\mathbf{r} - \mathbf{e}_i) \cdot \mathcal{CN}_{\mathbf{C}}(\mathbf{r}_0 - \mathbf{e}_i), \quad (35)$$

for all \mathbf{r} and \mathbf{r}_i . Please refer to [49, Appendix D] for a detailed proof. \square

To assess the performance of the proposed positioning method, the CRLB is derived based on the pdf (32). For an unbiased estimator, the estimation variance of the exact CFR \mathbf{r}_0 of location \mathbf{p}_0 is bounded by its CRLB, which is the inverse of the Fisher Information Matrix (FIM) $\mathbf{I}(\mathbf{r}_0)$. Under regularity conditions, the FIM is defined by [22]:

$$\mathbf{I}(\mathbf{r}_0) = -\mathbb{E} \left[\frac{\partial^2 \ln h(\mathbf{r})}{\partial \mathbf{r}_0 \partial \mathbf{r}_0^T} \right]. \quad (36)$$

The second order partial derivative of (32) with respect to \mathbf{r}_0 is expressed as (37) (in the bottom of next page). Note that the constant terms are neglected. It is evident that only the last two terms on the right-hand side are functions of variable \mathbf{r} . In this paper, we leave out the case where $\mathbf{r}_i = \mathbf{r}_0, \forall i$. For clarity of representation, we consolidate the remaining invariable terms (with respect to \mathbf{r}) of (37) into $i(\mathbf{r}_0)$. Thus, the FIM can be formulated by (38). Recalling the relationship $\mathbf{r}_j = \mathbf{D}_j \boldsymbol{\theta}'$, it is important to note that the FIM is essentially a function of the reflection coefficients $\boldsymbol{\theta}'$. This implies that the performance of localization varies under different configurations of RIS. This property, not previously considered in the literature, holds the potential for achieving improved positioning performance.

In this section, our goal is to derive the minimum CRLB. Instead of directly obtaining the CRLB, we focus on its inverse relation with the FIM, aiming to enhance the FIM, as suggested in [50]. It is important to note that both CRLB and FIM are discussed in the scope of positive definiteness of matrix. The close relationship between the FIM and the selection of \mathbf{r}_j becomes evident. Based on the assumption that all Gaussian components share the same covariance matrix $\boldsymbol{\Sigma}$, a fundamental conclusion can be drawn: at the point of maximum FIM, all \mathbf{r}_j converge to the same optimal solution (or set), denoted as \mathbf{r}^* , i.e., $\mathbf{r}_j = \mathbf{r}^*, \forall j = 1, \dots, L$. Consequently, we reformulate the FIM as (39). It can be observed that when \mathbf{r}_j approaches

\mathbf{r}_0 , the FIM converges to

$$\begin{aligned} \mathbf{I}_0 &= \lim_{\mathbf{r}_j \rightarrow \mathbf{r}_0} \mathbf{I}(\mathbf{r}_0; \boldsymbol{\theta}') \\ &= 2\boldsymbol{\Gamma}_0^{-1} + \frac{2}{L+1} \boldsymbol{\Sigma}^{-1} - \frac{2L}{L+1} \mathbf{C}^{-1} - \frac{4L}{(L+1)^2} \boldsymbol{\Sigma}^{-1} \mathbf{E} \boldsymbol{\Sigma}^{-1}. \end{aligned} \quad (40)$$

Additionally, as $\|\mathbf{C}^{-\frac{1}{2}}(\mathbf{r}_j - \mathbf{r}_0)\|_2$ tends to infinity, the FIM becomes:

$$\mathbf{I}_\infty = \lim_{\|\mathbf{C}^{-\frac{1}{2}}(\mathbf{r}_j - \mathbf{r}_0)\|_2 \rightarrow \infty} \mathbf{I}(\mathbf{r}_0; \boldsymbol{\theta}') = 2\boldsymbol{\Gamma}_0^{-1} + 2\boldsymbol{\Sigma}^{-1}. \quad (41)$$

Accounting for the definition of the limit operation, we can deduce that both \mathbf{r}_0 and the set $\{\mathbf{r}_j : \mathbf{I}(\mathbf{r}_0; \boldsymbol{\theta}') = \mathbf{I}_\infty\}$ are stationary points of $\mathbf{I}(\mathbf{r}_0; \boldsymbol{\theta}')$. Notably, the latter set represents a suboptimal solution for maximizing the FIM. This conclusion aligns with the intuitive understanding that positioning performance improves when interference from other locations is minimized, and worsens when all locations are closely grouped together. However, obtaining the global optimum can be challenging due to the complex expression involved. The conventional method of setting the partial derivative of $\mathbf{I}(\mathbf{r}_0; \boldsymbol{\theta}')$ with respect to \mathbf{r}_j equal to $\mathbf{0}$ leads to a transcendental equation, the solution of which is generally not in a closed form. Moreover, considering the limitations in the capabilities of RIS, even if the optimal solution can be determined, it remains challenging to ascertain the corresponding reflection coefficients. Specifically, the following series of equations may result in an empty feasible set for $\boldsymbol{\theta}'$:

$$\mathbf{D}_j \boldsymbol{\theta}' = \mathbf{r}^*, \text{ s.t. } |\theta'_m| = 1, \forall j = 1, 2, \dots, L, \forall m \in \mathcal{M}. \quad (42)$$

Building upon the analysis, it is considered that separate neighboring locations to improve positioning performance. Subsequently, a CRLB for unbiased estimators is obtained as:

$$\text{cov}(\hat{\mathbf{r}}_0) \geq \frac{1}{2} (\boldsymbol{\Gamma}_0^{-1} + \boldsymbol{\Sigma}^{-1})^{-1} = \frac{1}{2} \mathbf{E}, \quad (43)$$

where $\text{cov}(\cdot)$ denotes the covariance matrix of the input vector. For a geometric-based positioning method incorporated with the prior information, the CRLB is formulated as

$$\begin{aligned} \text{cov}(\hat{\mathbf{p}}_0) &\geq (\boldsymbol{\Gamma}^{-1} + \boldsymbol{\Sigma}_0^{-1})^{-1} \\ &= \boldsymbol{\Gamma} (\boldsymbol{\Gamma} + \boldsymbol{\Sigma}_0)^{-1} \boldsymbol{\Sigma}_0 = \boldsymbol{\Sigma}_0 - \boldsymbol{\Sigma}_0 (\boldsymbol{\Gamma} + \boldsymbol{\Sigma}_0)^{-1} \boldsymbol{\Sigma}_0, \end{aligned} \quad (44)$$

where $\boldsymbol{\Sigma}_0 (\boldsymbol{\Gamma} + \boldsymbol{\Sigma}_0)^{-1}$ is also recognized as the famous Kalman gain. Here, $\boldsymbol{\Gamma}$ is the covariance matrix of the geometric positioning method, which measures the same spread as our method in the virtual positioning space. Typically, the determinant of the covariance matrix is used to describe the spread of a random variable, known as generalized variance [51]. In this context, the following relations hold:

$$\det(\boldsymbol{\Gamma}_0) = \det(\boldsymbol{\Gamma}), \quad (45)$$

$$\det(\boldsymbol{\Sigma}_0) = \det \left(\boldsymbol{\Sigma} + \frac{1}{L+1} \sum_{i=0}^L (\mathbf{r}_j - \bar{\mathbf{r}})(\mathbf{r}_j - \bar{\mathbf{r}})^H \right), \quad (46)$$

where $\bar{\mathbf{r}} = \sum_{i=0}^L \mathbf{r}_j / (L+1)$ represents the mean of the Gaussian mixture of (29). The initial RIS coefficients are set the same for each element to simulate a usual NLOS link. It is important to note that the CRLB in (44) represents the lowest bound achievable by conventional geometric-based methods. For specific methods like those relying on RSS or AoA detection [52], the corresponding Jacobian matrix of the transit function must be multiplied by the FIM, a process that typically results in a degradation in performance.

V. SIMULATIONS

A. Simulation Setup

The considered simulation setup, as shown in Fig. 5, involves a BS equipped with N_T antennas at the center of the cell. The precoding vector is calculated by the typical MRT algorithm to reduce computational complexity. Randomly distributed single-antenna users (totaling K) are placed in both outdoor and cuboid indoor areas, with a higher indoor concentration. A

$$\begin{aligned} \frac{\partial^2 \ln h(\mathbf{r})}{\partial \mathbf{r}_0 \partial \mathbf{r}_0^T} &= \frac{-\partial^2 \ln \left(\sum_{j=0}^L \mathcal{CN}_{\mathbf{C}}(\mathbf{r}_0 - \mathbf{r}_j) \right) + \partial^2 \ln \left(\mathcal{CN}_{\mathbf{r}_0}(\mathbf{r} - \mathbf{r}_0) \right) + \partial^2 \ln \left(\sum_{j=0}^L \mathcal{CN}_{\boldsymbol{\Sigma}}(\mathbf{r} - \mathbf{r}_j) \right)}{\partial \mathbf{r}_0 \partial \mathbf{r}_0^T} \\ &= - \frac{4 \sum_{j=1}^L \mathcal{CN}_{\mathbf{C}}(\mathbf{r}_0 - \mathbf{r}_j) \mathbf{C}^{-1} (\mathbf{r}_0 - \mathbf{r}_j) (\mathbf{r}_0 - \mathbf{r}_j)^H \mathbf{C}^{-1} - 2 \sum_{j=1}^L \mathcal{CN}_{\mathbf{C}}(\mathbf{r}_0 - \mathbf{r}_j) \mathbf{C}^{-1}}{\sum_{j=0}^L \mathcal{CN}_{\mathbf{C}}(\mathbf{r}_0 - \mathbf{r}_j)} \\ &\quad + \frac{4 \left(\sum_{j=1}^L \mathcal{CN}_{\mathbf{C}}(\mathbf{r}_0 - \mathbf{r}_j) \mathbf{C}^{-1} (\mathbf{r}_0 - \mathbf{r}_j) \right) \left(\sum_{j=1}^L \mathcal{CN}_{\mathbf{C}}(\mathbf{r}_0 - \mathbf{r}_j) \mathbf{C}^{-1} (\mathbf{r}_0 - \mathbf{r}_j) \right)^H}{\left(\sum_{j=0}^L \mathcal{CN}_{\mathbf{C}}(\mathbf{r}_0 - \mathbf{r}_j) \right)^2} \\ &\quad - 2\boldsymbol{\Gamma}_0^{-1} + \frac{4\mathcal{CN}_{\boldsymbol{\Sigma}}(\mathbf{r} - \mathbf{r}_0) \boldsymbol{\Sigma}^{-1} (\mathbf{r} - \mathbf{r}_0) (\mathbf{r} - \mathbf{r}_0)^H \boldsymbol{\Sigma}^{-1} - 2\mathcal{CN}_{\boldsymbol{\Sigma}}(\mathbf{r} - \mathbf{r}_0) \boldsymbol{\Sigma}^{-1}}{\sum_{j=0}^L \mathcal{CN}_{\boldsymbol{\Sigma}}(\mathbf{r} - \mathbf{r}_j)} \\ &\quad - \frac{4\mathcal{CN}_{\boldsymbol{\Sigma}}^2(\mathbf{r} - \mathbf{r}_0) \boldsymbol{\Sigma}^{-1} (\mathbf{r} - \mathbf{r}_0) (\mathbf{r} - \mathbf{r}_0)^H \boldsymbol{\Sigma}^{-1}}{\left(\sum_{j=0}^L \mathcal{CN}_{\boldsymbol{\Sigma}}(\mathbf{r} - \mathbf{r}_j) \right)^2}. \end{aligned} \quad (37)$$

$$\begin{aligned}
 \mathbf{I}(\mathbf{r}_0) &= -i(\mathbf{r}_0) + \int_{\mathcal{C}} \frac{4\mathcal{CN}_{\Sigma}^2(\mathbf{r} - \mathbf{r}_0)\Sigma^{-1}(\mathbf{r} - \mathbf{r}_0)(\mathbf{r} - \mathbf{r}_0)^{\text{H}}\Sigma^{-1} \cdot \mathcal{CN}_{\Gamma_0}(\mathbf{r} - \mathbf{r}_0)}{\sum_{j=0}^L \mathcal{CN}_{\Sigma}(\mathbf{r} - \mathbf{r}_j) \cdot \sum_{j=0}^L \mathcal{CN}_{\mathbf{C}}(\mathbf{r}_0 - \mathbf{r}_j)} d\mathbf{r} \\
 &\quad - \int_{\mathcal{C}} \frac{(4\mathcal{CN}_{\Sigma}(\mathbf{r} - \mathbf{r}_0)\Sigma^{-1}(\mathbf{r} - \mathbf{r}_0)(\mathbf{r} - \mathbf{r}_0)^{\text{H}}\Sigma^{-1} - 2\mathcal{CN}_{\Sigma}(\mathbf{r} - \mathbf{r}_0)\Sigma^{-1}) \mathcal{CN}_{\Gamma_0}(\mathbf{r} - \mathbf{r}_0)}{\sum_{j=0}^L \mathcal{CN}_{\mathbf{C}}(\mathbf{r}_0 - \mathbf{r}_j)} d\mathbf{r} \\
 &= -i(\mathbf{r}_0) - \frac{\mathcal{CN}_{\mathbf{C}}(\mathbf{0})}{\sum_{j=0}^L \mathcal{CN}_{\mathbf{C}}(\mathbf{r}_0 - \mathbf{r}_j)} (4\Sigma^{-1}\mathbf{E}\Sigma^{-1} - 2\Sigma^{-1}) \\
 &\quad + \int_{\mathcal{C}} \frac{4\mathcal{CN}_{\Sigma}^2(\mathbf{r} - \mathbf{r}_0)\Sigma^{-1}(\mathbf{r} - \mathbf{r}_0)(\mathbf{r} - \mathbf{r}_0)^{\text{H}}\Sigma^{-1} \cdot \mathcal{CN}_{\Gamma_0}(\mathbf{r} - \mathbf{r}_0)}{\sum_{j=0}^L \mathcal{CN}_{\Sigma}(\mathbf{r} - \mathbf{r}_j) \cdot \sum_{j=0}^L \mathcal{CN}_{\mathbf{C}}(\mathbf{r}_0 - \mathbf{r}_j)} d\mathbf{r}.
 \end{aligned} \tag{38}$$

$$\begin{aligned}
 \mathbf{I}(\mathbf{r}_0; \theta') &= \frac{-2L\mathcal{CN}_{\mathbf{C}}(\mathbf{r}_0 - \mathbf{r}_j)\mathbf{C}^{-1}}{L\mathcal{CN}_{\mathbf{C}}(\mathbf{r}_0 - \mathbf{r}_j) + \mathcal{CN}_{\mathbf{C}}(\mathbf{0})} + \frac{4L\mathcal{CN}_{\mathbf{C}}(\mathbf{r}_0 - \mathbf{r}_j)\mathbf{C}^{-1}(\mathbf{r}_0 - \mathbf{r}_j)(\mathbf{r}_0 - \mathbf{r}_j)^{\text{H}}\mathbf{C}^{-1}}{(L\mathcal{CN}_{\mathbf{C}}(\mathbf{r}_0 - \mathbf{r}_j) + \mathcal{CN}_{\mathbf{C}}(\mathbf{0}))^2} \\
 &\quad + 2\Gamma_0^{-1} - \frac{\mathcal{CN}_{\mathbf{C}}(\mathbf{0})}{L\mathcal{CN}_{\mathbf{C}}(\mathbf{r}_0 - \mathbf{r}_j) + \mathcal{CN}_{\mathbf{C}}(\mathbf{0})} (4\Sigma^{-1}\mathbf{E}\Sigma^{-1} - 2\Sigma^{-1}) \\
 &\quad + \frac{4\mathcal{CN}_{\mathbf{C}}(\mathbf{0})\Sigma^{-1}}{(L\mathcal{CN}_{\mathbf{C}}(\mathbf{r}_0 - \mathbf{r}_j) + \mathcal{CN}_{\mathbf{C}}(\mathbf{0}))} \int_{\mathcal{C}} \frac{\mathcal{CN}_{\Sigma}(\mathbf{r} - \mathbf{r}_0)\mathcal{CN}_{\mathbf{E}}(\mathbf{r} - \mathbf{r}_0) \cdot (\mathbf{r} - \mathbf{r}_0)(\mathbf{r} - \mathbf{r}_0)^{\text{H}}}{L\mathcal{CN}_{\Sigma}(\mathbf{r} - \mathbf{r}_j) + \mathcal{CN}_{\Sigma}(\mathbf{r} - \mathbf{r}_0)} d\mathbf{r}\Sigma^{-1}.
 \end{aligned} \tag{39}$$

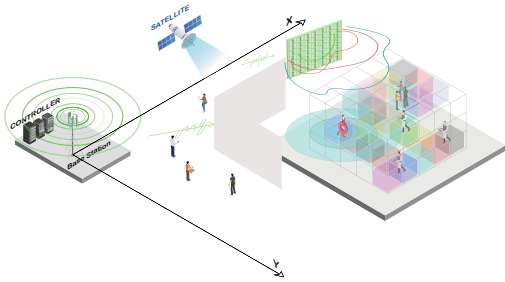


Fig. 5. Simulation environment setup.

RIS is appropriately deployed adjacent to the indoor area to establish transmission links for indoor users whose direct BS link is obstructed. Additionally, GNSS provides coarse prior information for indoor users. The cuboid indoor area is divided into blocks of dimensions $d \times d \times d$ for localization. In each realization of the channel, a specific subset of users with QoS requirements and another subset with positioning demands is randomly selected.

The cascaded channel matrix, \mathbf{G} , follows the IEEE 802.11b indoor propagation model [53]. This model characterizes the channel as a frequency-selective fading channel, incorporating an exponentially decaying power delay profile with a root-mean-square delay spread. The initial channel of user-RIS-BS and user-BS are randomly generated at blocks where the physical distance between any two blocks exceeds the correlation distance. Subsequently, the channels for the remaining locations are obtained by interpolation [54] to preserve spatial consistency [55]. The average number of taps in the impulse response is capped at $L_{\max} = 6$. The covariance matrices for the prior information and additive noise in the frequency domain, as well as the covariance matrices for the prior information and equivalent noise in the physical space, are represented as $\Sigma = \sigma^2\mathbf{I}_N$, $\Gamma_0 = \gamma_0^2\mathbf{I}_N$, $\Sigma_0 = \sigma_0^2\mathbf{I}_3$, $\Gamma = \gamma^2\mathbf{I}_3$, respectively. The average received SNR for indoor

users is defined as $\mathbb{E}_i[\|\mathbf{G}_i\theta\|_2^2]/N\gamma^2$. As the users are randomly distributed, we adopt the SNR of the user in the center of the cuboid area, as illustrated in Fig. 5, as the reference SNR. This reference level, denoted as SNR, is utilized in the subsequent simulations.

For indoor users, we assume that the LoS link directly from the BS is obstructed. All the results are obtained after averaging over 50 independent random channel realizations. The default system parameters are summarized in Table I. Customized parameters related to each subsection will be specified subsequently.

 TABLE I
 SYSTEM PARAMETERS

Parameters	Value
Carrier center frequency	2.4 GHz
Number of sub-carriers and pilot carriers	128 and 8
Default number of RIS elements	32
Number of users, and with QoS requirements	15 dB and 4 ~ 7 dB
Default QoS constraint, R_k	1.5 bps/Hz
Path loss exponent, α	2.5
Bound of channel estimation error	0.1
Variance of σ_0^2 and γ_0^2	5 dB and 10 dB
Indoor region size (m^3)	$9 \times 9 \times 3$
Penalty factor	1×10^{-3}
Converge tolerance	1×10^{-3}

B. Positioning Accuracy Evaluation

In Fig 6, we present and compare the positioning accuracy of different schemes in terms of root mean squared error (RMSE). The RSS-based positioning is realized with the methodology in [20]. The CRLB curves of both the conventional geometric-based method and the proposed two-stage scheme serve as baselines, establishing the bounds for positioning accuracy. Notably, the CRLB curves of the proposed positioning framework outperform all other cases, especially in low SNR conditions. This phenomenon showcases the superiority of the introduced

correlation dispersion property. The ultimate CRLB curve is obtained by (43). The number of Gaussian kernels in (29) is set $L = 12$. The optimized CRLB curve is obtained by (39), which provides a more stringent bound.

In this subsection, we set aside the QoS constraint in (10b) to evaluate the performance of the embedded positioning function. Moreover, we consider the case when (10a) is reduced to

$$(10a) \Rightarrow \min_{\Delta \mathbf{G}'} \|\mathbf{r}_{i_0, \mathcal{P}} - \mathbf{r}_{j, \mathcal{P}}\|_2^2 \geq d, j \in \mathcal{U}_{i_0}. \quad (47)$$

This single constraint means that we only consider the positioning of a specific location. This also leads support to our theoretical bound derivation of (43). For the case when all general constraints are considered, a degradation in positioning accuracy is clearly observed, especially when the SNR is relatively high. In comparison to the conventional RSS-based positioning method, the proposed strategy shows superiority, particularly in scenarios with low SNR. Conversely, under high SNR conditions, geometric-based methods demonstrate improved positioning accuracy as LoS paths become more distinguishable.

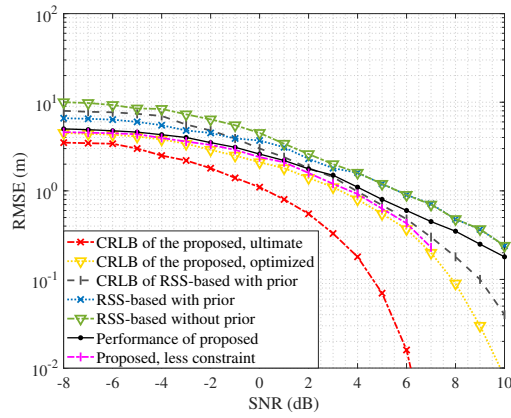


Fig. 6. Performance evaluation and comparison of the proposed scheme, number of RIS elements $M = 32$, number of pilot carriers $N_p = 8$, and variance of the prior information $\sigma_0^2 = 5$ dB.

In conclusion, the proposed framework performs better than conventional methods, capitalizing on distinct spatial consistencies in two different positioning spaces. In contrast, conventional geometric-based methods take advantage of comparatively less gain from the prior information, given the inherent similarity between the prior information and the methods themselves. Building upon these observations, we have validated the introduced correlation dispersion characteristic.

C. Positioning Performance Vesus QoS Requirements

Fig. 7 depicts the positioning performance in relation to the achievable data rate defined in (9). Other system parameters follow the default settings and the reference SNR is set to 10 dB. The number of communication users with specific requirements is randomly varied from 4 to 7 to simulate the dynamic of the communication system. As observed in Fig. 7, there is a gradual degradation in positioning accuracy for the proposed method as QoS requirement becomes more stringent. This is attributed to

both the RIS and the antenna array being optimized to enhance the received signal, resulting in higher SNR than initially designed. The embedded positioning function benefits from the improved propagation channel gain, leading to improved positioning accuracy. This observation emphasizes that the interconnection between the communication system and the embedded function cannot solely understood as a power allocation problem. Owing to the dynamic number of QoS requirements, the curves exhibit fluctuation with the increase of required data rates, especially when the rates conditions are strict.

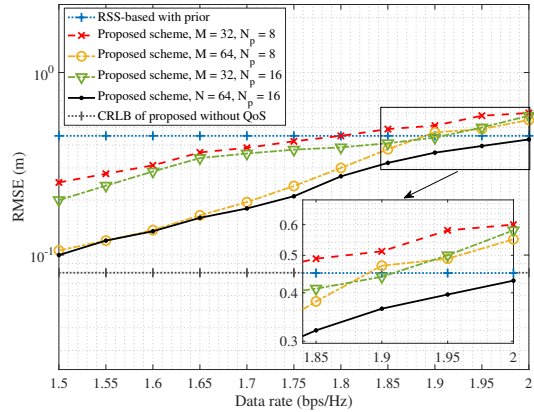


Fig. 7. Positioning accuracy versus communication requirements, variance of prior information $\sigma_0^2 = 5$ dB, SNR = 8 dB.

For the case with more RIS elements, i.e., $M = 64$, $N_p = 8$, the embedded positioning function acquires an improvement due to the redundancy in the RIS configuration for communication needs. For the case with more pilot carriers, i.e., $M = 32$, $N_p = 16$, the improvement is less pronounced as the overall SNR is low, and the capabilities of RIS are limited. However, the additional dimensionality provides a more detailed resolution. In the following, we will dig deeper into the relationship between the number of RIS elements and the number of pilot carriers.

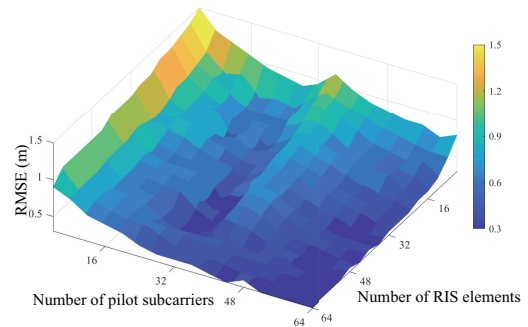


Fig. 8. Positioning accuracy versus the number of RIS elements and number of pilot carriers, SNR = 5 dB, $\sigma_0^2 = 5$ dB, no QoS.

D. Impact from Different System Settings

In Fig. 8, we explore the impact of the number of RIS elements and the length of the pilot subcarriers, without considering explicit QoS constraints. The variance of the prior information is set to 5 dB and the reference signal SNR is set 5 dB. When the number of pilot carriers is fixed, a consistent positive impact on the positioning performance is observed with an increase in the number of RIS elements. However, when the number of RIS elements is fixed, the monotonic relationship between the increase in RIS elements and the improvement in accuracy only holds when the number of RIS elements is considerably large. Notably, there is a discernible set of stationary points where the accuracy of positioning deteriorates with the escalating number of pilot subcarriers. Also, a gradual enhancement in positioning accuracy is evident with the increase of RIS elements. This phenomenon is primarily attributed to the insufficiency of reshaping the distribution of location in the positioning space when the number of RIS elements is relatively small. Nevertheless, as the number of pilot subcarriers increases, a more detailed fingerprint can be obtained, thereby facilitating improved positioning accuracy.

In summary, optimal positioning performance is achieved at specific points where the number of RIS elements and the number of pilot subcarriers match optimally. Beyond these points, there is a risk of degradation in performance, as they may counteract each other. Generally, an augmentation in the number of RIS elements consistently proves advantageous for the system.

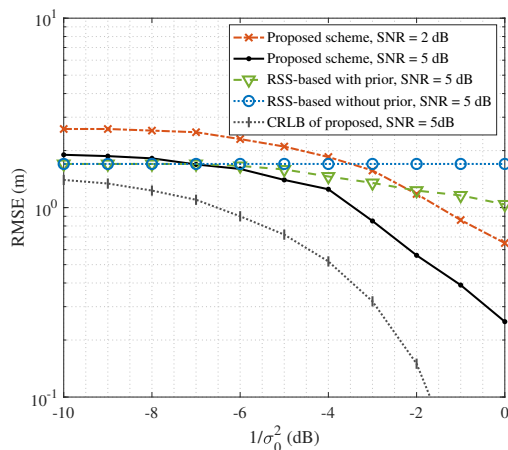


Fig. 9. Positioning accuracy versus the variance of prior information, $\sigma_0^2 = 5$ dB, number of RIS elements $M = 32$, number of pilot carriers $N_p = 8$.

E. Positioning with Prior Information

The combination of prior information in this paper results in an even smaller variance than both the variance of the prior information and the additive noise of the received signal. In Fig. 9, we illustrate the positioning performance with decreasing variance of the prior information. When the variance of the prior information is relatively large, it contributes insufficient information to narrow down the potential area of the user or localize the user accurately. Consequently, the both curves of

the proposed method reach to the upper bound that equals to the bound where there is no prior information. A noticeable improvement is observed earlier for the proposed scheme with $\text{SNR} = 5$ dB compared to $\text{SNR} = 2$ dB. In contrast, the conventional RSS-based method achieves similar improvement only when the prior information is relatively large. Specifically, to achieve meter-level accuracy, a 3 dB disparity is noted compared to the proposed scheme when SNR is set 5 dB.

In conclusion, despite a noticeable gap due to the presence of numerous constraints, the proposed methods consistently outperform the traditional approach when there is an increase in the prior information. It emphasizes the core idea of the proposed scheme that substantial improvement can be achieved when the location information captures different aspects.

VI. CONCLUSION

In this paper, we explored the ability of RIS to reshape the wireless environment in the frequency domain. Commencing with an integrated communication and positioning design based on CFR fingerprints, we proposed a two-stage positioning framework. The introduction of the prior information and its transformation into the positioning domain unveils a novel spatial correlation dispersion property. This property plays a crucial role in enhancing positioning performance, particularly in low SNR conditions. The CRLB of the proposed scheme was examined to theoretically validate this property. Extensive simulation results demonstrated that the proposed schemes achieve significant performance in terms of positioning accuracy, theoretical explanation, and communication assurance.

REFERENCES

- [1] C.-X. Wang, X. You, X. Gao, X. Zhu, Z. Li, C. Zhang, H. Wang, Y. Huang, Y. Chen, H. Haas, J. S. Thompson, E. G. Larsson, M. D. Renzo, W. Tong, P. Zhu, X. Shen, H. V. Poor, and L. Hanzo, "On the road to 6G: Visions, requirements, key technologies, and testbeds," *IEEE Commun. Surveys & Tutorials*, vol. 25, no. 2, pp. 905–974, 2023.
- [2] E. Basar, M. Di Renzo, J. De Rosny, M. Debbah, M.-S. Alouini, and R. Zhang, "Wireless communications through reconfigurable intelligent surfaces," *IEEE Access*, vol. 7, pp. 116 753–116 773, 2019.
- [3] Q. Wu and R. Zhang, "Towards smart and reconfigurable environment: Intelligent reflecting surface aided wireless network," *IEEE Commun. Mag.*, vol. 58, no. 1, pp. 106–112, 2020.
- [4] G. C. Alexandropoulos, K. Stylianopoulos, C. Huang, C. Yuen, M. Bennis, and M. Debbah, "Pervasive machine learning for smart radio environments enabled by reconfigurable intelligent surfaces," *Proceedings of the IEEE*, vol. 110, no. 9, pp. 1494–1525, 2022.
- [5] E. C. Strinati, G. C. Alexandropoulos, H. Wymeersch, B. Denis, V. Sciancalepore, R. D’Errico, A. Clemente, D.-T. Phan-Huy, E. De Carvalho, and P. Popovski, "Reconfigurable, intelligent, and sustainable wireless environments for 6G smart connectivity," *IEEE Commun. Mag.*, vol. 59, no. 10, pp. 99–105, 2021.
- [6] E. C. Strinati, G. C. Alexandropoulos, V. Sciancalepore, M. Di Renzo, H. Wymeersch, D.-T. Phan-Huy, M. Crozzoli, R. D’Errico, E. De Carvalho, P. Popovski, P. Di Lorenzo, L. Bastianelli, M. Belouar, J. E. Mascolo, G. Gradoni, S. Phang, G. Leroosey, and B. Denis, "Wireless environment as a service enabled by reconfigurable intelligent surfaces: The RISE-6G perspective," in *2021 Joint European Conf. Netw. and Commun. & 6G Summit (EuCNC/6G Summit)*, 2021, pp. 562–567.
- [7] F. Liu, L. Zheng, Y. Cui, C. Masouros, A. P. Petropulu, H. Griffiths, and Y. C. Eldar, "Seventy years of radar and communications: The road from separation to integration," *IEEE Signal Process. Mag.*, vol. 40, no. 5, pp. 106–121, 2023.
- [8] Z. Wang, K. Han, J. Jiang, Z. Wei, G. Zhu, Z. Feng, J. Lu, and C. Meng, "Symbiotic sensing and communications towards 6G: Vision, applications, and technology trends," in *2021 IEEE 94th Veh. Technol. Conf. (VTC2021-Fall)*, 2021, pp. 1–5.

- [9] E. C. Strinati and S. Barbarossa, "6G networks: Beyond Shannon towards semantic and goal-oriented communications," *Comp. Netw.*, vol. 190, p. 107930, 2021.
- [10] R. Koirala, B. Denis, D. Dardari, and B. Uguen, "Localization bound based beamforming optimization for multicarrier mmwave mimo," in *2017 14th Workshop on Positioning, Navigation and Communications (WPNC)*, 2017, pp. 1–6.
- [11] R. Koirala, B. Denis, B. Uguen, D. Dardari, and H. Wymeersch, "Localization and communication resource budgeting for multi-user mm-wave mimo," in *2019 16th Workshop on Positioning, Navigation and Communications (WPNC)*, 2019, pp. 1–5.
- [12] Y. Xu, Z. Wang, P. Liu, J. Chen, S. Han, C. Yu, and J. Yu, "Accuracy analysis and improvement of visible light positioning based on VLC system using orthogonal frequency division multiple access," *Optics Express*, vol. 25, no. 26, pp. 32 618–32 630, 2017.
- [13] M. Liu, S. Xia, M. Xiong, M. Xu, W. Fang, and Q. Liu, "Integrated communication and positioning with resonant beam," *IEEE Trans. Wireless Commun.*, vol. 21, no. 11, pp. 9186–9199, 2022.
- [14] N. Williams, G. Wu, and P. Closas, "Impact of positioning uncertainty on eco-approach and departure of connected and automated vehicles," in *2018 IEEE/ION Position, Location and Navigation Symposium (PLANS)*, 2018, pp. 1081–1087.
- [15] S. Baek, D. Kim, M. Tesanovic, and A. Agiwal, "3gpp new radio release 16: Evolution of 5g for industrial internet of things," *IEEE Commun. Mag.*, vol. 59, no. 1, pp. 41–47, 2021.
- [16] C. Ren and L. Liu, "Toward full passive internet of things: Symbiotic localization and ambient backscatter communication," *IEEE Internet of Things Journal*, vol. 10, no. 22, pp. 19 495–19 506, 2023.
- [17] H. Wymeersch, J. He, B. Denis, A. Clemente, and M. Juntti, "Radio localization and mapping with reconfigurable intelligent surfaces: Challenges, opportunities, and research directions," *IEEE Veh. Mag.*, vol. 15, no. 4, pp. 52–61, 2020.
- [18] J. He, H. Wymeersch, T. Sanganpuak, O. Silven, and M. Juntti, "Adaptive beamforming design for mmwave RIS-aided joint localization and communication," in *2020 IEEE Wireless Commun. Netw. Conf. Workshops (WCNCW)*, 2020, pp. 1–6.
- [19] C. L. Nguyen, O. Georgiou, G. Gradoni, and M. Di Renzo, "Wireless fingerprinting localization in smart environments using reconfigurable intelligent surfaces," *IEEE Access*, vol. 9, pp. 135 526–135 541, 2021.
- [20] H. Zhang, H. Zhang, B. Di, K. Bian, Z. Han, C. Xu, D. Zhang, and L. Song, "RSS fingerprinting based multi-user outdoor localization using reconfigurable intelligent surfaces," in *2021 15th International Symposium on Medical Inf. Commun. Technol. (ISMICT)*, 2021, pp. 167–172.
- [21] H. Zhang, J. Hu, H. Zhang, B. Di, K. Bian, Z. Han, and L. Song, "Metaradar: Indoor localization by reconfigurable metamaterials," *IEEE Trans. Mobile Comp.*, vol. 21, no. 8, pp. 2895–2908, 2022.
- [22] S. M. Kay, *Fundamentals of statistical signal processing: estimation theory*. Prentice-Hall, Inc., 1993.
- [23] F. Ademaj, S. Schwarz, T. Berisha, and M. Rupp, "A spatial consistency model for geometry-based stochastic channels," *IEEE Access*, vol. 7, pp. 183 414–183 427, 2019.
- [24] H. Zhang, L. Song, Z. Han, and H. V. Poor, "Spatial equalization before reception: Reconfigurable intelligent surfaces for multi-path mitigation," in *ICASSP 2021 - 2021 IEEE International Conference on Acoustics, Speech and Signal Processing (ICASSP)*, 2021, pp. 8062–8066.
- [25] E. Arslan, I. Yildirim, F. Kilinc, and E. Basar, "Over-the-air equalization with reconfigurable intelligent surfaces," *IET Communications*, vol. 16, no. 13, pp. 1486–1497, 2022.
- [26] S. Lin, B. Zheng, G. C. Alexandropoulos, M. Wen, F. Chen, and S. Mumtaz, "Adaptive transmission for reconfigurable intelligent surface-assisted OFDM wireless communications," *IEEE J. Sel. Areas Commun.*, vol. 38, no. 11, pp. 2653–2665, 2020.
- [27] Z. Yang, Z. Zhou, and Y. Liu, "From RSSI to CSI: Indoor localization via channel response," *ACM Computing Surveys (CSUR)*, vol. 46, no. 2, pp. 1–32, 2013.
- [28] D. Tse and P. Viswanath, *Fundamentals of wireless communication*. Cambridge university press, 2005.
- [29] Q. Shi, M. Razaviyayn, Z.-Q. Luo, and C. He, "An iteratively weighted mmse approach to distributed sum-utility maximization for a mimo interfering broadcast channel," *IEEE Trans. Signal Process.*, vol. 59, no. 9, pp. 4331–4340, 2011.
- [30] X. Yu, J.-C. Shen, J. Zhang, and K. B. Letaief, "Alternating minimization algorithms for hybrid precoding in millimeter wave mimo systems," *IEEE J. Sel. Topics Signal Process.*, vol. 10, no. 3, pp. 485–500, 2016.
- [31] K. Feng, X. Li, Y. Han, and Y. Chen, "Joint beamforming optimization for reconfigurable intelligent surface-enabled MISO-OFDM systems," *China Communications*, vol. 18, no. 3, pp. 63–79, 2021.
- [32] J. Torres-Sospedra, R. Montoliu, S. Trilles, Ó. Belmonte, and J. Huerta, "Comprehensive analysis of distance and similarity measures for Wi-Fi fingerprinting indoor positioning systems," *Expert Systems with Applications*, vol. 42, no. 23, pp. 9263–9278, 2015.
- [33] Y. Li, Z. Han, Z. Liu, H. Wang, C. You, and W. Liu, "A multilevel feature and structure prior information-based positioning approach for catenary support components," *IEEE Trans. Instrum. Meas.*, vol. 70, pp. 1–13, 2021.
- [34] C. You, B. Zheng, and R. Zhang, "Intelligent reflecting surface with discrete phase shifts: Channel estimation and passive beamforming," in *ICC 2020 - 2020 IEEE Int. Conf. Commun. (ICC)*, 2020, pp. 1–6.
- [35] D. W. K. Ng, E. S. Lo, and R. Schober, "Robust beamforming for secure communication in systems with wireless information and power transfer," *IEEE Trans. Wireless Commun.*, vol. 13, no. 8, pp. 4599–4615, 2014.
- [36] H. Yang, W.-D. Zhong, C. Chen, A. Alphones, and P. Du, "QoS-driven optimized design-based integrated visible light communication and positioning for indoor IoT networks," *IEEE J. IoT*, vol. 7, no. 1, pp. 269–283, 2020.
- [37] U. L. Wijewardhana, S. Joshi, M. Codreanu, and M. Latva-aho, "Worst-case weighted sum-rate maximization for MISO downlink systems with imperfect channel knowledge," in *2013 Asilomar Conf. Signals, Syst. and Comp.*, 2013, pp. 1248–1252.
- [38] Z.-Q. Luo, J. F. Sturm, and S. Zhang, "Multivariate nonnegative quadratic mappings," *SIAM Journal on Optimization*, vol. 14, no. 4, pp. 1140–1162, 2004.
- [39] X. Yu, D. Xu, Y. Sun, D. W. K. Ng, and R. Schober, "Robust and secure wireless communications via intelligent reflecting surfaces," *IEEE J. Sel. Areas Commun.*, vol. 38, no. 11, pp. 2637–2652, 2020.
- [40] S. Wright, J. Nocedal *et al.*, "Numerical optimization," *Springer Science*, vol. 35, no. 67–68, p. 7, 1999.
- [41] T. Jiang and Y. Shi, "Over-the-air computation via intelligent reflecting surfaces," in *2019 IEEE Global Commun. Conf. (GLOBECOM)*, 2019, pp. 1–6.
- [42] M. Grant and S. Boyd, "Cvx: Matlab software for disciplined convex programming, version 2.1," 2014.
- [43] Y. Sun, P. Babu, and D. P. Palomar, "Majorization-minimization algorithms in signal processing, communications, and machine learning," *IEEE Trans. Signal Process.*, vol. 65, no. 3, pp. 794–816, 2017.
- [44] I. Pólik and T. Terlaky, *Interior Point Methods for Nonlinear Optimization*. Berlin, Heidelberg: Springer Berlin Heidelberg, 2010, pp. 215–276. [Online]. Available: https://doi.org/10.1007/978-3-642-11339-0_4
- [45] T. N. NGOC, A. KHENCHAF, and F. COMBLET, "Evaluating process and measurement noise in extended Kalman filter for GNSS position accuracy," in *2019 13th European Conference on Antennas and Propagation (EuCAP)*, 2019, pp. 1–5.
- [46] C. Luschki and B. Mulgrew, "Nonparametric trellis equalization in the presence of non-gaussian interference," *IEEE Trans. Commun.*, vol. 51, no. 2, pp. 229–239, 2003.
- [47] E. Parzen, "On estimation of a probability density function and mode," *The Annals of Mathematical Statistics*, vol. 33, no. 3, pp. 1065–1076, 1962.
- [48] C. Genest, "A characterization theorem for externally Bayesian groups," *The Annals of Statistics*, pp. 1100–1105, 1984.
- [49] R. P. S. Mahler, *Statistical Multisource-Multitarget Information Fusion*. USA: Artech House, Inc., 2007.
- [50] C. R. Rao and M. Statistiker, *Linear statistical inference and its applications*. Wiley New York, 1973, vol. 2.
- [51] A. Sengupta, "Generalized variance," *Encyclopedia of statistical sciences*, vol. 3, no. 1, 2004.
- [52] D. Niculescu and B. Nath, "Ad hoc positioning system (APS) using AoA," in *IEEE INFOCOM 2003. Twenty-second Annual Joint Conference of the IEEE Computer and Communications Societies (IEEE Cat. No.03CH37428)*, vol. 3, 2003, pp. 1734–1743 vol.3.
- [53] A. Borrelli, C. Monti, M. Vari, and F. Mazzenga, "Channel models for IEEE 802.11b indoor system design," in *2004 IEEE International Conference on Communications (IEEE Cat. No.04CH37577)*, vol. 6, 2004, pp. 3701–3705 Vol.6.
- [54] 3GPP R1-161622, "Spatial consistency modeling in drop based model," March 2016, [online] Available: <http://www.3gpp.org>.
- [55] 3GPP TR 38.901, "Study on channel model for frequencies from 0.5 to 100 GHz (release 17)," Mar. 2022, [online] Available: <http://www.3gpp.org>.